

Article

Upcycling of Cr-Containing Sulfate Waste into Efficient FeCrO₃/Fe₂O₃ Catalysts for CO₂ Hydrogenation Reaction

Yongqi Liu ¹, Shasha Chu ¹, Yuebing Xu ^{2,*} , Xinyu Chen ¹, Hao Zhou ¹, Jinlin Li ¹, Yanjie Ren ³ and Xintai Su ^{1,*}

¹ Guangdong Provincial Key Laboratory of Solid Wastes Pollution Control and Recycling, School of Environment and Energy, South China University of Technology, Guangzhou 510006, China

² School of Chemical and Material Engineering, Jiangnan University, Wuxi 214122, China

³ Xinjiang Qinghua Energy Group Co., Ltd., Yining County 835100, China

* Correspondence: xuyuebing@jiangnan.edu.cn (Y.X.); suxintai@scut.edu.cn (X.S.)

Abstract: Upcycling Cr-containing sulfate waste into catalysts for CO₂ hydrogenation reaction benefits both pollution mitigation and economic sustainability. In this study, FeCrO₃/Fe₂O₃ catalysts were successfully prepared by a simple hydrothermal method using Cr-containing sodium sulfate (Cr-SS) as a Cr source for efficient conversion and stable treatment of Cr. The removal rate of Cr in Cr-SS can reach 99.9% at the optimized hydrothermal conditions. When the synthesized catalysts were activated and used for the CO₂ hydrogenation reaction, a 50% increase in CO₂ conversion was achieved compared with the catalyst prepared by impregnation with a comparable amount of Cr. According to the extraction and risk assessment code (RAC) of the Reference Office of the European Community Bureau (BCR), the synthesized FeCrO₃/Fe₂O₃ is risk-free. This work not only realizes the detoxification of the Cr-SS but transfers Cr into stable FeCrO₃ for application in a catalytic field, which provides a strategy for the harmless disposal and resource utilization of Cr-containing hazardous waste.

Keywords: Cr-containing sodium sulfate; FeCrO₃/Fe₂O₃ catalyst; CO₂ hydrogenation reaction; detoxification



Citation: Liu, Y.; Chu, S.; Xu, Y.; Chen, X.; Zhou, H.; Li, J.; Ren, Y.; Su, X. Upcycling of Cr-Containing Sulfate Waste into Efficient FeCrO₃/Fe₂O₃ Catalysts for CO₂ Hydrogenation Reaction. *Materials* **2024**, *17*, 1598. <https://doi.org/10.3390/ma17071598>

Academic Editor: Ellie Uzunova

Received: 5 March 2024

Revised: 24 March 2024

Accepted: 29 March 2024

Published: 31 March 2024



Copyright: © 2024 by the authors. Licensee MDPI, Basel, Switzerland. This article is an open access article distributed under the terms and conditions of the Creative Commons Attribution (CC BY) license (<https://creativecommons.org/licenses/by/4.0/>).

1. Introduction

Cr-containing sodium sulfate (Cr-SS) is a by-product in the production process of the chrome salt industry. Cr (VI) in Cr-SS has the characteristics of high mobility, high toxicity, and carcinogenesis [1,2]. If it is discharged into the environment without proper treatment, it will pose a serious threat to the ecological environment and human health. In fact, Cr has been designated as hazardous waste in the China National Hazardous Waste List (2016), making the safe treatment and resource utilization of Cr-SS a pressing issue within chromium-related industries.

Currently, treatment methods for Cr-containing waste are categorized into harmless [3] and extraction methods [4]. Commonly employed techniques include wet reduction [5], high-temperature roasting [6], bioremediation [7–9], immobilization/stabilization [10,11], and physico-chemical extraction methods [4,12–14]. Among these methods, wet reduction and physico-chemical extraction are commonly used disposal measures. Wet reduction involves the use of acids or bases to transfer Cr (VI) from the solid phase to the liquid phase and then chemically reduce it to Cr (III), which is less toxic. Although this method is simple, it usually produces acid–base waste liquid and consumes a large amount of reducing agent [15]. The physico-chemical extraction method achieves sufficient extraction of Cr by controlling the phase transition of solid particles [16]. Although this method realizes the effective extraction of chromium, it has not been fully explored in the utilization of resources. Considering that Cr is a strategic metal resource, the annual waste of Cr resources due to inefficient practices is enormous [17,18]. Therefore, it is urgent to develop an efficient, stable, and economical method to recover chromium from Cr-containing sodium sulfate.

We propose the idea of detoxifying Cr from Cr-containing sodium sulfate (Cr-SS) and selectively converting it into functional materials to achieve a balance between environmental and economic considerations. Since Cr exists mainly in the form of Fe-Cr crystals in the natural environment [19], the conversion of Cr into stable Fe-Cr crystals can significantly reduce its ecotoxicity due to oxidation. On the other hand, iron–chromium oxide (FeCrO_3) has a similar molecular formula to ilmenite, which display excellent chemical stability, thermal stability, magnetic properties, and specific catalytic capabilities [20–22]. Therefore, if the Cr in Cr-SS can be selectively converted into FeCrO_3 by direct reaction with iron, the simultaneous detoxification and stabilization of Cr can be effectively achieved, which provides a new strategy for the resource utilization of Cr-containing wastes. Some studies have mentioned the hydrothermal conversion of Cr(VI) to stable ferrite. Lan [23] synthesized FeCr_2O_4 by hydrothermal treatment of chromium-containing wastewater, while Xie [24] applied hydrothermal treatment to chromium sludge and synthesized FeCr_2O_4 for advanced persulfate oxidation. However, there has been no research on the conversion of chromium from Cr-containing waste to FeCrO_3 for high-value utilization.

In this study, Cr (VI) detoxification and the preparation of $\text{FeCrO}_3/\text{Fe}_2\text{O}_3$ catalytic material were realized by a hydrothermal process using Cr-SS as raw material. The obtained material is activated and used for a carbon dioxide hydrogenation reaction. The research objectives include the following: (1) investigating the effects of different hydrothermal treatment conditions on the fixation and stabilization of Cr. (2) The prepared $\text{FeCrO}_3/\text{Fe}_2\text{O}_3$, $\text{Cr}/\text{Fe}_2\text{O}_3$, and Fe_2O_3 were analyzed utilizing analytical characterization methods. (3) Elucidating the mechanism of Cr(VI) conversion to FeCrO_3 . (4) Conducting CO_2 hydrogenation experiments on $\text{FeCrO}_3/\text{Fe}_2\text{O}_3$, $\text{Cr}/\text{Fe}_2\text{O}_3$, and Fe_2O_3 to investigate differences in catalytic performance. (5) Determining the speciation of Cr in different Fe-Cr materials using the European Community Bureau of Reference (BCR) method and assessing their environmental risks using the risk assessment code (RAC) method. This study provides a convenient method for the efficient detoxification of Cr-SS and fixation of Cr elements, and also offers a feasible strategy for the effective disposal and resource utilization of Cr-containing solid waste.

2. Experimental

2.1. Materials

The Cr-SS was obtained from Chongqing Minfeng Chemical Co., Ltd. (Chongqing, China). It is a by-product of the process used to prepare chromate and dichromate from chrome ore using the alkali method. The collected samples were dried at 80 °C, crushed, and sieved to ensure uniform compositions. After ICP determination, the total Cr content in Cr-SS is 1.03 mg/g. The chemical reagents used in this study included anhydrous sodium sulfite (Na_2SO_3 , AR, 99%), ferric sulfate ($\text{Fe}_2(\text{SO}_4)_3$, AR, 99%), sodium sulfate (Na_2SO_4 , AR, 99%), and urea ($\text{CO}(\text{NH}_2)_2$, AR, 99%) purchased from Aladdin Reagent Co., Ltd. (Shanghai, China). Deionized water was used in all the experiments. All chemicals were used as received and without further purification. Unless otherwise noted, all samples tested herein were screened through a 200 mesh (0.074 mm) sieve.

2.2. Experimental

2.2.1. Preparation of $\text{FeCrO}_3/\text{FeOOH}$ and $\text{FeCrO}_3/\text{Fe}_2\text{O}_3$

Firstly, 1.0 g of Cr-SS was dissolved in 20 mL of deionized water, then Cr(VI) was utterly reduced to Cr(III) by adding Na_2SO_3 . Simultaneously, $\text{Fe}_2(\text{SO}_4)_3$ and $\text{CO}(\text{NH}_2)_2$ were introduced to form a homogeneous solution, transferred into a 100 mL Teflon-lined stainless autoclave, and maintained at 180 °C for 12 h. After air-cooling to room temperature, the precipitate was filtered and washed with deionized water and anhydrous alcohol several times and then dried in an oven at 80 °C for 10 h. The dried product is denoted as $\text{FeCrO}_3/\text{FeOOH}$. Finally, the $\text{FeCrO}_3/\text{Fe}_2\text{O}_3$ was obtained by calcinating the $\text{FeCrO}_3/\text{FeOOH}$ powder in air at 500 °C for 2 h with a 10 °C/min heating rate (the process of calcination at 500 °C for 2 h was regarded as high-temperature activation).

The solution was collected after hydrothermal reaction, and then dried to obtain the sodium salt after removing Cr (Cr-SS-AR). After ICP testing, the Cr content in Cr-SS-AR is 3.18×10^{-4} mg/g. The Cr removal rate of the method can be calculated to be 99.9% based on Formula (1).

$$\text{Cr removal rate} = (c(\text{Cr-SS}) - c(\text{Cr-SS-AR})) / c(\text{Cr-SS}) \times 100\% \quad (1)$$

2.2.2. Preparation of Fe₂O₃ and Cr/Fe₂O₃

To compare the catalytic performance of FeCrO₃/Fe₂O₃ material in CO₂ hydrogenation synthesis, a control sample was prepared using Na₂SO₄ instead of Cr-SS. The following steps were followed to obtain Fe₂O₃ and Cr/Fe₂O₃ materials.

Cr-SS was replaced with Na₂SO₄ under the same experimental conditions as FeCrO₃/Fe₂O₃. The final product obtained is Fe₂O₃.

An isovolumetric impregnation method was employed, using the previously obtained Fe₂O₃ as the impregnation cocatalyst. The impregnated cocatalyst was dried in an oven at 120 °C for 2 h, and 1.0 g was taken for the determination of water absorption. Based on the water absorption of Fe₂O₃, Na₂CrO₄ was used as the Cr source, and deionized water was used as the solvent to formulate the impregnation solution with the corresponding concentration, so as to ensure that the final Cr loading of the catalyst was 0.3%. A total of 1.0 g of dried sample was put into an eggplant-shaped bottle, adding the calculated amount of impregnation solution, impregnated at room temperature for 1 h, stirring every 10 min to ensure full impregnation, then vacuum drying at the end of impregnation for 12 h to obtain a red powder, and the obtained red powder was put into a muffle furnace, and the temperature was raised to 500 °C at a rate of 10 °C/min and kept for 2 h, to obtain the final catalyst product, named as Cr/Fe₂O₃.

2.3. Characterization

The total metal concentrations were analyzed using an inductively coupled plasma emission spectrometer (ICP-OES, AvioTM200, PerkinElmer, Waltham, MA, USA). The Cr(VI) concentrations were quantified at 540 nm using a UV-vis spectrophotometer (UV2600, Shimadzu, Kyoto, Japan) based on the diphenylcarbazide colorimetric method (GB7467 [25] and GB/T15555.4-1995 [26]). The mineral phase compositions of the samples were determined using an X-ray diffractometer (XRD, D8Advance, Bruker, Saarbrücken, Germany) in continuous scanning mode with Cu-K α radiation ($\lambda = 1.5418 \text{ \AA}$, 40 kV, 40 mA). The samples' microstructure, morphology, and elemental analysis were examined using a scanning electron microscope equipped with an energy-dispersive X-ray spectrometer (SEM-EDS, Sigma300, Zeiss, Oberkochen, UK). The microstructure of the samples was observed using a transmission electron microscope (TEM, FEI Talos F200X, Waltham, MA, USA) in STEM mode at 200 kV. The valence changes of heavy metals on the sample surface were analyzed using X-ray photoelectron spectroscopy (XPS, Escalab 250Xi, Thermo Fisher Scientific, Waltham, MA, USA).

2.4. CO₂ Hydrogenation Test

Catalytic performance evaluation of the synthesized catalyst for CO₂/H₂ methanation synthesis was conducted in a fixed-bed reactor. A 0.3 g sample of fresh catalyst and a 2.0 g sample of quartz sand were evenly blended and loaded into the reaction tube. The reaction was conducted under constant H₂ flow rate conditions (100 mL/min). The temperature was increased at a rate of 2 °C/min until reaching 400 °C for a reduction period of 4 h. Subsequently, the temperature was lowered to 240 °C for evaluation under atmospheric pressure. The feed gas composition was V(H₂): V(CO₂) = 3:1 with a 100 mL/min flow rate. The Agilent (Santa Clara, CA, USA) GC-7820A gas chromatograph equipped with a thermal conductivity detector (TCD) and a flame ionization detector (FID) was used to analyze the online feed gas and gas products. The TCD, equipped with a Porapak Q column and an MS 5A packed column, was used to analyze components such as CO₂, CO,

CH₄, etc. The FID, equipped with an Rt-Q-Bond column, was used to analyze hydrocarbon products ranging from C₂ to C₇. CO₂ conversion (X_{CO_2} , %) and product selectivity (S , %) were calculated [27] as shown in Equations (2)–(5):

$$X_{CO_2} = \frac{A_{CO_2in} - A_{CO_2out}}{A_{CO_2in}} \times 100\% \quad (2)$$

$$S_{CO} = \frac{A_{CO\ out}}{A_{CO\ in} - A_{CO\ out}} \times 100\% \quad (3)$$

$$S_{CH_4} = \frac{A_{CH_4out}}{A_{CH_4\ in} - A_{CH_4out}} \times 100\% \quad (4)$$

$$S_{C_2-C_7} = 100\% - S_{CH_4} - S_{CO} \quad (5)$$

In the equations, X_{CO_2} represents the conversion rate of CO₂. S_{CO} , S_{CH_4} , and $S_{C_2-C_7}$ represent the selectivity of each component. A_{CO_2} , A_{CO} , and A_{CH_4} represent the molar concentration of each component, and the subscripts in and out represent the feed gas and the outlet gas, respectively.

2.5. Stability Test

Different forms of Cr in FeCrO₃/Fe₂O₃ and Cr/Fe₂O₃ were extracted by a modified BCR four-step extraction method [28]. A sample weighing 0.8 g was mixed with 32 mL of a 0.1 mol/L acetic acid solution. The mixture was shaken for 16 h and then centrifuged to obtain extract 1 (exchangeable fraction F1) and residue 1. In residue 1, 32 mL of a 0.5 mol/L hydroxylamine hydrochloride solution was added, followed by shaking for 16 h. The mixture was centrifuged to obtain extract 2 (reducible fraction F2) and residue 2. For residue 2, 8 mL of an 8.8 mol/L hydrogen peroxide solution was added, and the mixture was heated until the volume was reduced to 1 mL. Then, 25 mL of a 1 mol/L ammonium acetate solution was added, followed by shaking for 16 h. The mixture was centrifuged to obtain extract 3 (oxidizable fraction F3) and residue 3. The dried sample from residue 3 was placed in a digestion bottle and mixed with 8 mL of aquaregia. The mixture was allowed to digest at room temperature for 5 h and then diluted to obtain extract 4 (residual fraction F4).

Formula (6) can be used to calculate the proportion of metal instability in the total content of the material, so as to assess the environmental risk level after the material is discarded [29].

$$RAC = F1\ \text{fraction} / \text{Total amount of heavy metals} \quad (6)$$

3. Results and Discussion

3.1. Detoxification and Targeted Transfer of Cr in Cr-SS

We determined the effect of conditions on Cr removal from Cr-SS by controlling the hydrothermal temperature, hydrothermal time, and the amounts of CO(NH₂)₂ and Fe₂(SO₄)₃; the detailed information can be found in the).

As shown in Figure S1, when the mass ratio of Cr-SS, Fe₂(SO₄)₃, and CO(NH₂)₂ is 1 g:1 g:0.6 g, and the hydrothermal conditions are 180 °C and 12 h, the best Cr removal effect can be obtained. The XRD pattern of Cr-SS (Figure S2a) shows that the main phase is Na₂SO₄, and no crystalline compound of Cr was found. However, as shown in Figure S2b, Cr-SS is a yellow granular substance. This indicates that in Cr-SS, the content of Cr is relatively low, or Cr exists as amorphous Na₂CrO₄. After processing, the XRD pattern of Cr-SS-AR (Figure S2c) shows that the main phases of Cr-SS are Na₂SO₄ and (NH₄)₂SO₄. The optical image of Cr-SS-AR (Figure S2d) shows the appearance of white particle crystals, indicating that Cr in Cr-SS has been removed. The Cr content in Cr-SS decreased from 41.2 mg/L to 1.27 × 10⁻² mg/L before and after hydrothermal treatment, and no Fe content was detected (Table S1). In conclusion, the removal rate of Cr is 99.9% when the method

is used for detoxification of Cr-SS, which is well-matched to the similar literature (see Table S2 for details on what the literature compares) [23,24,30–32].

The cocatalysts were prepared using Cr-SS and Na_2SO_4 under the above optimum dechromiumization conditions and the XRD patterns and SEM images are shown in Figure 1. As shown in Figure 1, the characteristic peak of the material prepared by Na_2SO_4 corresponded to FeOOH, and the material was named FeOOH, and a new characteristic peak corresponding to FeCrO_3 appeared in the material prepared by Cr-SS, and the material was named $\text{FeCrO}_3/\text{FeOOH}$. By comparing the XRD spectra of the two materials, it was found that the peak corresponding to FeOOH in $\text{FeCrO}_3/\text{FeOOH}$ was shifted to a lower angle. According to the Bragg equation ($2d\sin\theta = n\lambda$), doping with heteroatoms of larger atomic radii increases the lattice constant, which leads to a shift in the diffraction peaks of the phases [33], which can indicate that Cr has been successfully doped into FeOOH to form FeCrO_3 . Surface morphology analyses were carried out on both FeOOH and $\text{FeCrO}_3/\text{FeOOH}$, as shown in Figure 1b, short rod-shaped crystals are observed on the surface of FeOOH, whereas the surface of $\text{FeCrO}_3/\text{FeOOH}$ (Figure 1c) shows a regular hexahedral structure, and the size of the crystal size is also significantly increased. This suggests that Cr doping changes the surface morphology of the materials.

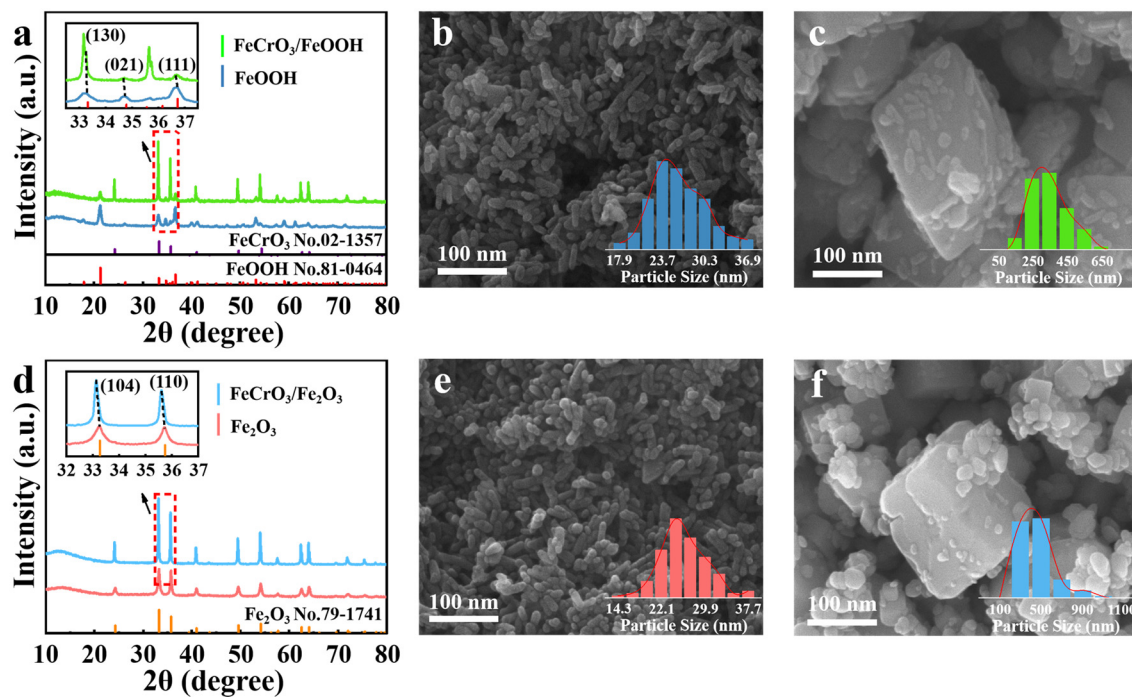


Figure 1. XRD patterns of (a) FeOOH and $\text{FeCrO}_3/\text{FeOOH}$ before high-temperature activation and (d) Fe_2O_3 and $\text{FeCrO}_3/\text{Fe}_2\text{O}_3$ after being activated at 500°C . SEM images of (b) FeOOH, (c) $\text{FeCrO}_3/\text{FeOOH}$, (e) Fe_2O_3 , and (f) $\text{FeCrO}_3/\text{Fe}_2\text{O}_3$.

FeOOH and $\text{FeCrO}_3/\text{FeOOH}$ were activated at high temperature, and the two materials were transformed into Fe_2O_3 and $\text{FeCrO}_3/\text{Fe}_2\text{O}_3$, respectively. Figure 1d shows the XRD patterns of Fe_2O_3 and $\text{FeCrO}_3/\text{Fe}_2\text{O}_3$. The inability to identify the characteristic peaks of FeCrO_3 alone may be due to the fact that the characteristic peaks of Fe_2O_3 are too strong, or due to the proximity of the characteristic peaks of FeCrO_3 and Fe_2O_3 . However, in $\text{FeCrO}_3/\text{Fe}_2\text{O}_3$, the characteristic peaks corresponding to the (110) and (104) crystal faces of Fe_2O_3 are shifted to a lower angle, suggesting that the material was successfully doped with chromium. Compared with $\text{FeCrO}_3/\text{Fe}_2\text{O}_3$, the diffraction peaks of pure Fe_2O_3 are wider (as shown in Figure 1e,f), which may be attributed to the larger grain size of $\text{FeCrO}_3/\text{Fe}_2\text{O}_3$, resulting in the reduction in internal stresses inside the crystal, which leads to the narrowing of the diffraction peaks. In addition, the original morphological features

of both Fe_2O_3 and FeCrO_3 remain intact after the high-temperature activation treatment, indicating no signs of sintering or melting. This result indicates that the materials have good thermal stability and are suitable for thermal catalyst synthesis.

XRD and SEM information for the Fe_2O_3 and $\text{Cr}/\text{Fe}_2\text{O}_3$ materials used for the comparison of catalytic properties can be found in the SI (Figures S4 and S5). Based on Figure S4, it is evident that the characteristic peaks of Fe_2O_3 completely align with the standard card, signifying that the prepared Fe_2O_3 material is a pure phase. The $\text{Cr}/\text{Fe}_2\text{O}_3$ obtained by the impregnation method did not show the characteristic peaks of the Cr phase, which may be caused by the low content of Cr and its uniform dispersion on the surface of the material. Nonetheless, the characteristic peaks corresponding to the Fe_2O_3 (104) and (110) crystal planes shift towards lower angles, indicating the successful loading of Cr onto Fe_2O_3 . It can be seen from Figure S5a–c that the Fe_2O_3 material has good crystallinity and uniform element distribution. Figure S5d shows that the $\text{Cr}/\text{Fe}_2\text{O}_3$ surface does not appear as a regular hexahedron like the $\text{FeCrO}_3/\text{Fe}_2\text{O}_3$ (Figure 1f) material, which indicates that Cr only uniformly covers the short rod-like crystals on the surface of the material.

TEM analysis reveals the presence of hexahedral-shaped Fe–Cr crystals on the surface of the Fe matrix, as depicted in Figure 2a. The HRTEM images (Figure 2b) were Fourier transformed to determine two sets of lattice spacings of 0.25 nm and 0.27 nm, matching the (110) and (104) planes of FeCrO_3 . From Figure 2c,e, it can be seen that the crystallinity of $\text{FeCrO}_3/\text{Fe}_2\text{O}_3$ is good. In addition, the EDX results (Figure 2g) indicate that the O, Fe, and Cr elements are uniformly distributed within the selected area of the nanocrystal.

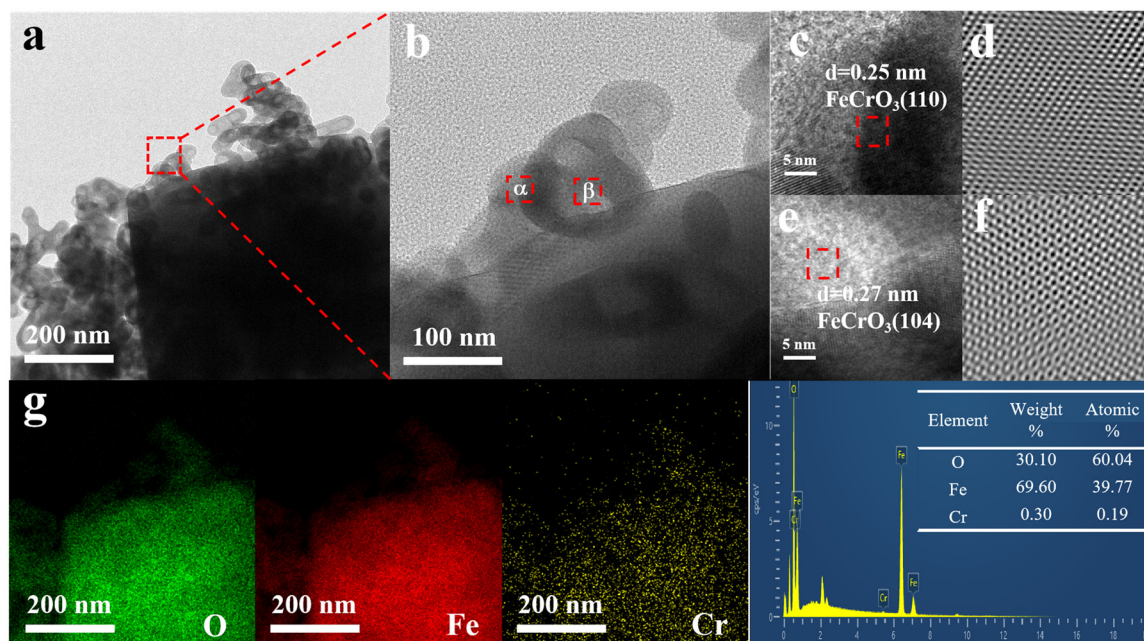


Figure 2. (a) TEM image, (b) HRTEM image, (c,d) IFFT image of the constituency α , (e,f) IFFT image of the constituency β , and (g) energy-dispersive X-ray spectroscopy (EDX) mapping images and spectra of $\text{FeCrO}_3/\text{Fe}_2\text{O}_3$.

The XPS spectrum of $\text{FeCrO}_3/\text{Fe}_2\text{O}_3$ is shown in Figure 3a. Three peaks at 531 eV, 577 eV, and 711 eV, corresponding to the binding energies of O 1s, Cr 2p, and Fe 2p, respectively, indicate the presence of O, Cr, and Fe elements. The O 1s XPS spectra shown in Figure 3b indicate that the peak at 530 eV may be attributed to lattice oxygen, while the peaks at 531.7 eV, 532.7 eV, and 533.7 eV are attributed to O–H, oxygen vacancies, and chemisorbed oxygen [34,35]. As shown in Figure 3c, the Cr 2p XPS peaks observed at 586 eV and 577 eV correspond to the Cr 2p_{1/2} and Cr 2p_{3/2} peaks [36]. The peaks at 576.5 eV and 578.1 eV are attributed to Cr^{3+} , which suggests that the valence state exists predominantly in the form of Cr^{3+} and that a small amount of Cr^{6+} may be the key to the

better catalytic performance of the material in later stages. As shown in Figure 3d, the Fe 2p XPS peaks observed at 725.1 eV and 711.6 eV correspond to the Fe 2p_{1/2} and Fe 2p_{3/2} peaks [37–39], respectively. In conclusion, during the crystallization process, Fe and Cr are mainly present as Fe³⁺ and Cr³⁺, which is consistent with the elemental valence state of FeCrO₃, and further proves that the combination of Cr and Fe forms stable FeCrO₃ crystals instead of FeCr₂O₄ crystals [40]. The XPS spectra of the Fe₂O₃ and Cr/Fe₂O₃ catalysts are detailed in SI (Figures S6 and S7). In Figure S6b, it can be determined that Fe₂O₃ contains lattice oxygen, O-H, oxygen vacancies, and chemisorbed oxygen, and from Figure S6c, it can be determined that Fe₂O₃ contains only Fe³⁺. As shown in Figure S7, Cr/Fe₂O₃ contains lattice oxygen, O-H, and oxygen vacancies, and no Cr⁶⁺ peak is detected in this material, which may be an important reason for inhibiting its catalytic performance.

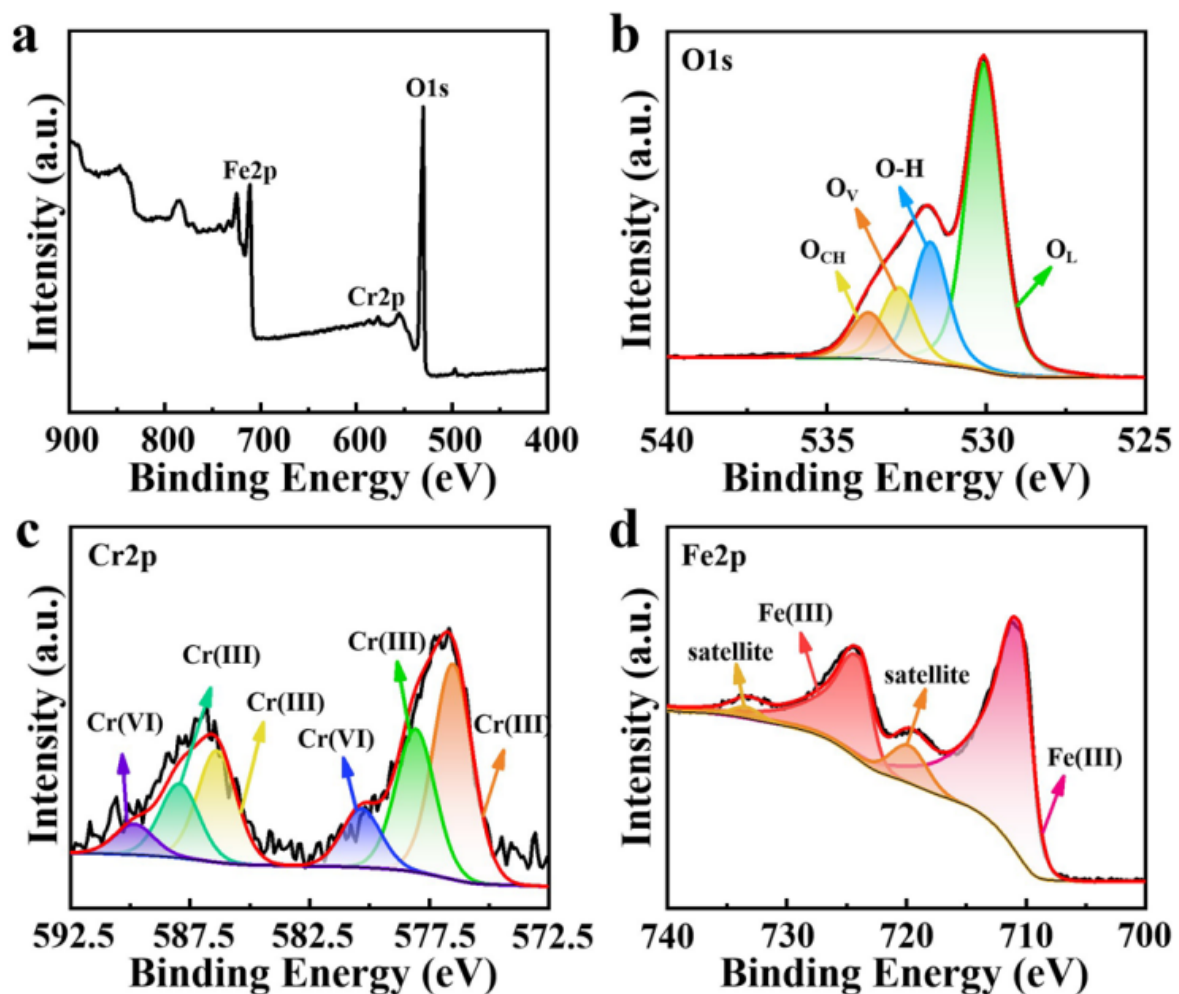


Figure 3. XPS spectra of FeCrO₃/Fe₂O₃. (a) Full survey spectrum, (b) O 1s, (c) Cr 2p, and (d) Fe 2p. (The red line is the fitting curve obtained after the peak separation of XPS.)

3.2. Formation Mechanism of FeCrO₃

The chemical formula for iron titanium-type crystals is FeMO₃ (M refers to metal elements), representing the substitution of a Fe atom in Fe₂O₃ with a metal atom M that possesses properties similar to Fe [41]. The proportion of metal cations in the crystals is influenced by factors such as the metal atoms' radius, valence state, and gap size [42]. Consequently, substitution phenomena can occur among metal atoms with comparable properties under specific physical and chemical conditions. Common ilmenite-type crystals include FeTiO₃, FeCrO₃, FeGeO₃, etc. [41,43,44]. Due to their similar atomic numbers (Fe-26 and Cr-24), Fe and Cr have analogous ionic radii and properties. Therefore, stable FeCrO₃

crystals can form when appropriate molar ratios and hydrothermal conditions are present. Using a proper amount of ferric sulfate as a cocatalyst powder not only accelerates the formation of the ferrite matrix but also enhances the presence of free Cr^{3+} , promotes its binding with FeOOH sites, and further accelerates the formation of FeCrO_3 .

In Figure 4, the detoxification mechanism of Cr(VI) from Cr-SS and its conversion into FeCrO_3 is illustrated. The Cr-SS solution contains a high concentration of free Cr^{6+} . Sodium sulfite (Na_2SO_3) provides SO_3^{2-} during the reaction process, reducing free Cr^{6+} in chromic acid to Cr^{3+} (see reaction Formula (7)). During the hydrothermal stage, $\text{CO(NH}_2)_2$ is gradually hydrolyzed to provide an alkaline environment for the reaction (see reaction Formula (8)). $\text{Fe}_2(\text{SO}_4)_3$, utilized as a cocatalyst powder, forms Fe(OH)_3 under alkaline conditions (see reaction Formula (9)). As the hydrothermal reaction progresses, Fe(OH)_3 begins to transform into FeOOH (see reaction Formula (10)). As shown in Figure S8, an iron matrix composed of Fe(OH)_3 is initially formed, and FeOOH grows on its surface as the hydrothermal reaction continues. In an alkaline environment, free Cr^{3+} first forms Cr(OH)_3 (see reaction Formula (11)). When Fe ions are abundant, under alkaline hydrothermal conditions, FeOOH and Cr(OH)_3 are converted to the target product FeCrO_3 at $180\text{ }^\circ\text{C}$ (see reaction Formula (12)).

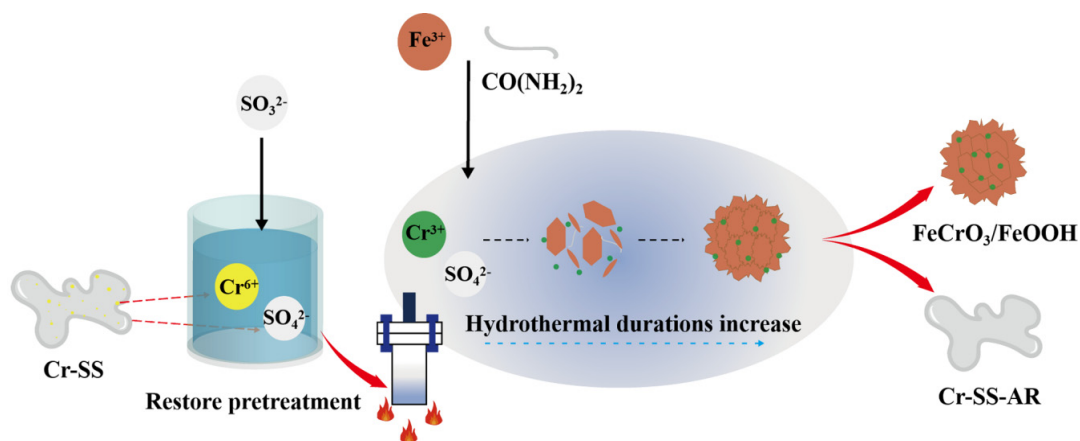
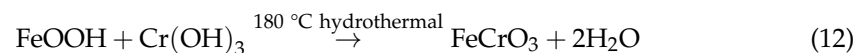
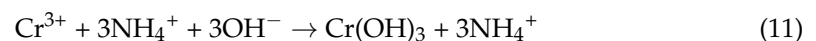
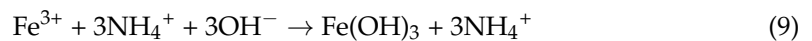
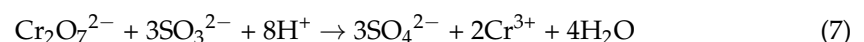


Figure 4. Schematic illustration of detoxification of Cr-SS and synthesis into $\text{FeCrO}_3/\text{FeOOH}$.

The chemical reaction formulas are described as follows:



3.3. CO_2 Hydrogenation Reaction Performance

As shown in Figure 5a, $\text{FeCrO}_3/\text{Fe}_2\text{O}_3$ exhibits higher CO_2 conversion compared to Fe_2O_3 and $\text{Cr}/\text{Fe}_2\text{O}_3$. With the increase in reaction time, the CO_2 conversion of $\text{FeCrO}_3/\text{Fe}_2\text{O}_3$ did not change significantly, indicating its good stability. The CO_2 conversion ability of $\text{Cr}/\text{Fe}_2\text{O}_3$ decreased in the first 2 h, then increased slowly, and reached the maximum at 8 h. This may be since Cr loaded by the impregnation method only deposits on the surface of the material, which inhibits the conversion of Fe_2O_3 to Fe-carbide and, thus, reduces the CO_2 conversion. However, with the increase in reaction time, some

chromium will be detached from the Fe_2O_3 surface, which may expose more iron sites, thus, improving the CO_2 conversion.

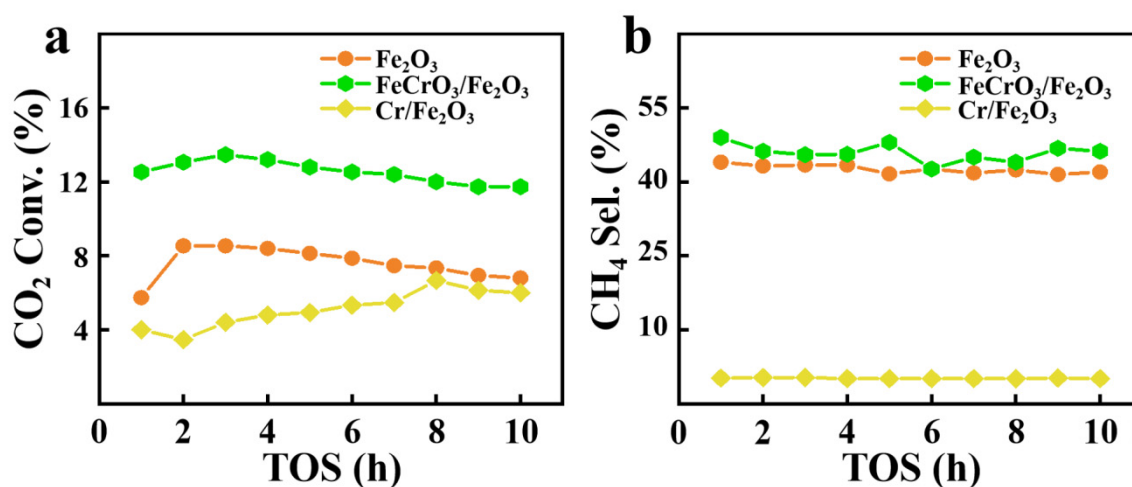


Figure 5. The (a) CO_2 conversion rate and (b) CH_4 selectivity rate of Fe_2O_3 , $\text{FeCrO}_3/\text{Fe}_2\text{O}_3$, and $\text{Cr}/\text{Fe}_2\text{O}_3$.

As can be seen in Figure 5b, $\text{FeCrO}_3/\text{Fe}_2\text{O}_3$ maintains a high CH_4 selectivity throughout the reaction period, further highlighting its excellent stability. The results also show that $\text{Cr}/\text{Fe}_2\text{O}_3$ lacks selectivity for CH_4 , while Fe_2O_3 has more than 40% selectivity for CH_4 . This suggests that a single Cr species loaded on the surface of Fe_2O_3 has low selectivity for CH_4 and even inhibits the original catalytic selectivity of the cocatalyst. As shown in Figure S8, the selectivity of $\text{FeCrO}_3/\text{Fe}_2\text{O}_3$ for the $\text{C}_2\text{--C}_7$ product is twice that of Fe_2O_3 . At the same time, the product selectivity of $\text{FeCrO}_3/\text{Fe}_2\text{O}_3$ did not change significantly with the increase in reaction time, indicating that the material had good catalytic stability. The poor CO_2 conversion and product selectivity of $\text{Cr}/\text{Fe}_2\text{O}_3$ may be due to the simple formation of CrO_x particles rather than the formation of catalytically active chromium species. $\text{FeCrO}_3/\text{Fe}_2\text{O}_3$ not only has a larger contact area but also prevents the cocatalyst from sintering by forming hexahedral crystals, which is conducive to the catalytic reaction. Meanwhile, we compared the performance of the catalysts prepared in this paper with that of the catalysts in the literature (see Table S3 for specific data) [27,45–48]. The results show that the low-temperature CO_2 hydrogenation catalyst prepared by Cr-SS had better CH_4 selectivity and certain CO_2 conversion ability compared with the catalyst prepared by pure reagents.

3.4. Stability Evaluation

In order to better understand the mobility, stability, and toxicity of Cr in $\text{FeCrO}_3/\text{Fe}_2\text{O}_3$ and $\text{Cr}/\text{Fe}_2\text{O}_3$ materials, an improved BCR method was used to determine the speciation of heavy metals in the samples, and toxicity risk assessment was conducted using the RAC method [49]. The content of different forms of Cr in $\text{FeCrO}_3/\text{Fe}_2\text{O}_3$ and $\text{Cr}/\text{Fe}_2\text{O}_3$ and the RAC value of the material are detailed in SI (Table S4).

As shown in Figure 6, the values of F1 and F2 in $\text{FeCrO}_3/\text{Fe}_2\text{O}_3$ are significantly lower than those in $\text{Cr}/\text{Fe}_2\text{O}_3$. The exchangeable metal form in the F1 part is usually considered the most easily transferable metal. Compared with $\text{FeCrO}_3/\text{Fe}_2\text{O}_3$, $\text{Cr}/\text{Fe}_2\text{O}_3$ contains significantly higher Cr content in the exchangeable state, indicating a higher potential environmental risk. At the same time, it can be seen from the figure that the proportion of easily transitive forms (F1 and F2) of Cr in $\text{FeCrO}_3/\text{Fe}_2\text{O}_3$ is relatively low, indicating that the directional conversion of Cr into FeCrO_3 through hydrothermal pathways can better fix Cr, increase the proportion of stable state (F3 and F4), and effectively reduce the environmental risk level of the material [50]. At the same time, as shown in Table S5, the Cr^{6+} content of $\text{FeCrO}_3/\text{Fe}_2\text{O}_3$ as an active site is very low, and the material exists in

the form of iron–chromium crystals, indicating that it is not easy to be oxidized and the risk of poisoning is very low. Additionally, the RAC value of $\text{FeCrO}_3/\text{Fe}_2\text{O}_3$ is below 1%, indicating it is a non-risk substance. In contrast, the RAC value of $\text{Cr}/\text{Fe}_2\text{O}_3$ is between 1–10%, and when the material is discarded and enters the natural environment, improper treatment can easily cause secondary environmental pollution.

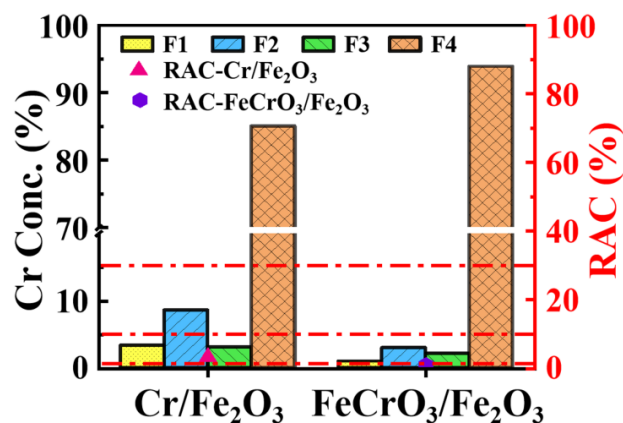


Figure 6. The different forms of Cr content and their RAC values in $\text{FeCrO}_3/\text{Fe}_2\text{O}_3$ and $\text{Cr}/\text{Fe}_2\text{O}_3$. (The red dash line corresponds to RAC values of different scales.)

4. Conclusions

In conclusion, this study introduces the direct conversion of Cr into $\text{FeCrO}_3/\text{Fe}_2\text{O}_3$ through a straightforward hydrothermal reaction utilizing Cr-containing sodium sulfate (Cr-SS) as the raw material, followed by its application in low-temperature CO_2 hydrogenation reactions. The incorporation of Cr prompts the transition of short rod-like crystals into hexahedral crystals, significantly increasing the crystal particle size. Moreover, the hydrothermal synthesis of FeCrO_3 preserves the original O-H, oxygen vacancies, and adsorbed oxygen content of Fe_2O_3 , ensuring the maintenance of its inherent catalytic performance. When employed in catalytic reactions, FeCrO_3 achieves a CO_2 conversion rate of 12.4% and a CH_4 selectivity of 45.9%, surpassing the performance of Fe_2O_3 and $\text{Cr}/\text{Fe}_2\text{O}_3$ used as controls in the study. Furthermore, the proposed mechanism and corresponding equations elucidate the directional conversion of Fe^{3+} and Cr^{3+} into FeCrO_3 during the hydrothermal process. Stability assessments conducted using the BCR and RAC methods confirm the risk-free nature of the FeCrO_3 materials. This study not only accomplishes the removal and stabilization of chromium in Cr-SS but also yields a catalyst suitable for low-temperature CO_2 hydrogenation reactions, presenting a valuable solution for the detoxification and recycling of chromium-containing wastes.

Supplementary Materials: The following supporting information can be downloaded at: <https://www.mdpi.com/article/10.3390/ma17071598/s1>. Figure S1: Total Cr content in hydrothermal solution at different (a) reaction temperature, (b) reaction time, (c) dosage of $\text{Fe}_2(\text{SO}_4)_3$ and (d) dosage of $\text{CO}(\text{NH}_2)_2$. Figure S2: (a) XRD pattern, (b) optical image of Cr-SS. (c) XRD pattern, (d) optical image of Cr-SS-AR. Figure S3: The overall morphology of (a–c) FeOOH and (d–f) $\text{FeCrO}_3/\text{FeOOH}$. Figure S4: XRD pattern of Fe_2O_3 and $\text{Cr}/\text{Fe}_2\text{O}_3$. Figure S5: SEM-EDX images (a–c) of Fe_2O_3 and SEM-EDX spectra (d–f) of $\text{Cr}/\text{Fe}_2\text{O}_3$. Figure S6: XPS spectra of Fe_2O_3 . (a) full survey spectrum, (b) O 1s and (c) Fe 2p. Figure S7: XPS spectra of $\text{Cr}/\text{Fe}_2\text{O}_3$. (a) full survey spectrum, (b) O 1s, (c) Cr 2p and (d) Fe 2p. Figure S8: SEM images of Cr-SS hydrothermal treatment for (a,b) 0.5 h, (c,d) 2 h, (e,f) 4 h, (g,h) 8 h and (i,j) 12 h. Figure S9: C_2 – C_7 products selectivity of Fe_2O_3 , $\text{FeCrO}_3/\text{Fe}_2\text{O}_3$, and $\text{Cr}/\text{Fe}_2\text{O}_3$. Table S1: Cr content in the Cr-SS before and after treatment. Table S2: The comparison between the traditional and this paper in Cr removal from Cr-containing wastes. Table S3: The comparison of CO_2 hydrogenation performance of different catalysts. Table S4: Different forms content and the RAC value of Cr in $\text{FeCrO}_3/\text{Fe}_2\text{O}_3$ and $\text{Cr}/\text{Fe}_2\text{O}_3$. Table S5: Chromium content in different valence states for $\text{FeCrO}_3/\text{Fe}_2\text{O}_3$ and $\text{Cr}/\text{Fe}_2\text{O}_3$.

Author Contributions: Y.L.: Methodology, data curation, writing—original draft, investigation, formal analysis. S.C.: Conceptualization, investigation, formal analysis. Y.X.: Experiment of CO₂ hydrogenation synthesis test, review. X.C.: Conceptualization, writing—review. H.Z.: Conceptualization, writing—review. J.L.: Catalyst preparation. Y.R.: Project administration, supervision. X.S.: Methodology, writing—review and editing, Project administration, funding acquisition. All authors have read and agreed to the published version of the manuscript.

Funding: This work was supported by the National Natural Science Foundation of China (no. 22176064), the National Key Research and Development Program of China (no. 2019YFA0210402), the Guangdong Science and Technology Program (no. 2020B1212010038), the Guangdong Province Regional Joint Fund-Youth Fund Project (no. 2022A1515110796), and the Guangzhou Basic and Applied Basic Research Project (no. 202201010463).

Data Availability Statement: Data are contained within the article and Supplementary Materials.

Conflicts of Interest: Author Yanjie Ren was employed by the company Xinjiang Qinghua Energy Group Co., Ltd. The remaining authors declare that the research was conducted in the absence of any commercial or financial relationships that could be construed as a potential conflict of interest.

References

1. Liu, W.; Li, J.; Zheng, J.; Song, Y.; Shi, Z.; Lin, Z.; Chai, L. Different Pathways for Cr(III) Oxidation: Implications for Cr(VI) Reoccurrence in Reduced Chromite Ore Processing Residue. *Environ. Sci. Technol.* **2020**, *54*, 11971–11979. [[CrossRef](#)] [[PubMed](#)]
2. Watts, M.P.; Coker, V.S.; Parry, S.A.; Patrick, R.A.D.; Thomas, R.A.P.; Kalin, R.; Lloyd, J.R. Biogenic nano-magnetite and nano-zero valent iron treatment of alkaline Cr(VI) leachate and chromite ore processing residue. *Appl. Geochem.* **2015**, *54*, 27–42. [[CrossRef](#)] [[PubMed](#)]
3. Yang, Y.; Shi, S.; Zhu, C.; Chen, X.; Hao, Y.; Yan, L.; Li, J.; Chen, X.; Chen, B.; Ma, X.; et al. Immobilization of chromium in real tannery sludge via heat treatment with coal fly ash. *Chemosphere* **2023**, *335*, 139180. [[CrossRef](#)] [[PubMed](#)]
4. Liu, W.; Zheng, J.; Ou, X.; Liu, X.; Song, Y.; Tian, C.; Rong, W.; Shi, Z.; Dang, Z.; Lin, Z. Effective Extraction of Cr(VI) from Hazardous Gypsum Sludge via Controlling the Phase Transformation and Chromium Species. *Environ. Sci. Technol.* **2018**, *52*, 13336–13342. [[CrossRef](#)] [[PubMed](#)]
5. Du, Y.; Chrysochoou, M. Chemistry and Leaching Behavior of Chromite Ore Processing Residue from the Soda Ash Process. *Environ. Eng. Sci.* **2018**, *35*, 1185–1193. [[CrossRef](#)]
6. Kim, E.; Spooren, J.; Broos, K.; Horckmans, L.; Quaghebeur, M.; Vrancken, K.C. Selective recovery of Cr from stainless steel slag by alkaline roasting followed by water leaching. *Hydrometallurgy* **2015**, *158*, 139–148. [[CrossRef](#)]
7. Guo, S.; Xiao, C.; Zheng, Y.; Li, Y.; Chi, R. Removal and potential mechanisms of Cr(VI) contamination in phosphate mining wasteland by isolated *Bacillus megatherium* PMW-03. *J. Clean. Prod.* **2021**, *322*, 129062. [[CrossRef](#)]
8. Bencheikh-Latmani, R.; Obratsova, A.; Mackey, M.R.; Ellisman, M.H.; Tebo, B.M. Toxicity of Cr(III) to *Shewanella* sp. strain MR-4 during Cr(VI) reduction. *Environ. Sci. Technol.* **2007**, *41*, 214–220. [[CrossRef](#)] [[PubMed](#)]
9. Field, E.K.; Blaskovich, J.P.; Peyton, B.M.; Gerlach, R. Carbon-dependent chromate toxicity mechanism in an environmental *Arthrobacter* isolate. *J. Hazard. Mater.* **2018**, *355*, 162–169. [[CrossRef](#)]
10. Fan, C.; Qian, J.; Yang, Y.; Sun, H.; Song, J.; Fan, Y. Green ceramsite production via calcination of chromium contaminated soil and the toxic Cr(VI) immobilization mechanisms. *J. Clean. Prod.* **2021**, *315*, 129062. [[CrossRef](#)]
11. Muhammad, F.; Xia, M.; Li, S.; Yu, X.; Mao, Y.; Muhammad, F.; Huang, X.; Jiao, B.; Yu, L.; Li, D. The reduction of chromite ore processing residues by green tea synthesized nano zerovalent iron and its solidification/stabilization in composite geopolymer. *J. Clean. Prod.* **2019**, *234*, 381–391. [[CrossRef](#)]
12. Srivastava, A.N.; Chakma, S. Bioavailability reduction of heavy metals through dual mode anaerobic Co-landfilling of municipal solid waste and industrial organic sludge. *Chem. Eng. J.* **2022**, *439*, 135725. [[CrossRef](#)]
13. Tardif, S.; Cipullo, S.; So, H.U.; Wragg, J.; Holm, P.E.; Coulon, F.; Brandt, K.K.; Cave, M. Factors governing the solid phase distribution of Cr, Cu and As in contaminated soil after 40 years of ageing. *Sci. Total Environ.* **2019**, *652*, 744–754. [[CrossRef](#)]
14. Trzonkowska, L.; Lesniewska, B.; Godlewska-Zylkiewicz, B. Development of Solid Phase Extraction Method Based on Ion Imprinted Polymer for Determination of Cr(III) Ions by ETAAS in Waters. *Water* **2022**, *14*, 529. [[CrossRef](#)]
15. Wang, X.; Zhang, J.; Wang, L.; Chen, J.; Hou, H.; Yang, J.; Lu, X. Long-term stability of FeSO₄ and H₂SO₄ treated chromite ore processing residue (COPR): Importance of H⁺ and SO₄²⁻. *J. Hazard. Mater.* **2017**, *321*, 720–727. [[CrossRef](#)]
16. Zheng, J.; Lv, J.; Liu, W.; Dai, Z.; Liao, H.; Deng, H.; Lin, Z. Selective recovery of Cr from electroplating nanosludge via crystal modification and dilute acid leaching. *Environ. Sci. -Nano* **2020**, *7*, 1593–1601. [[CrossRef](#)]
17. Kumar, P.; Patra, S.K.; Tripathy, S.K.; Sahu, N. Efficient utilization of nickel rich Chromite Ore Processing Tailings by carbothermic smelting. *J. Clean. Prod.* **2021**, *315*, 128046. [[CrossRef](#)]
18. Liu, W.; Zheng, J.; Wu, Z.; Liu, Z.; Lin, Z. The Application of Micro-Mechanism of Crystal Changes under the Surface/Interface Control in Treating Chromium-Containing Residues. *Prog. Chem.* **2017**, *29*, 1053–1061. [[CrossRef](#)]

19. Papassiopi, N.; Vaxevanidou, K.; Christou, C.; Karagianni, E.; Antipas, G.S.E. Synthesis, characterization and stability of Cr(III) and Fe(III) hydroxides. *J. Hazard. Mater.* **2014**, *264*, 490–497. [[CrossRef](#)]
20. Lacerda, L.H.d.S.; de Lazaro, S.R. A broad theoretical investigation of R-3, R3c, and R-3c polymorphs of FeCrO₃. *J. Am. Ceram. Soc.* **2020**, *103*, 5688–5699. [[CrossRef](#)]
21. Lacerda, L.H.S.; Lazaro, S.R.d. Surface and morphology investigation of FeCrO₃ material in ilmenite-, corundum- and lithium niobate-polymorphs. *Surf. Interfaces* **2021**, *22*, 100837. [[CrossRef](#)]
22. Ateia, E.E.; Soliman, F.S. Multiferroic properties of Gd/Er doped chromium ferrite nano sized particles synthesized by citrate auto combustion method. *Mater. Sci. Eng. B-Adv. Funct. Solid-State Mater.* **2019**, *244*, 29–37. [[CrossRef](#)]
23. Lan, Y.; Zhang, L.; Li, X.; Liu, W.; Su, X.; Lin, Z. Efficient immobilization and utilization of chromite ore processing residue via hydrothermally constructing spinel phase Fe²⁺(Cr³⁺_x, Fe³⁺_{2-x})O₄ and its magnetic separation. *Sci. Total Environ.* **2022**, *813*, 152637. [[CrossRef](#)] [[PubMed](#)]
24. Xie, D.; Chu, S.; Zhang, S.; Ivanets, A.; Zhang, L.; Su, X. Facile synthesis of Cr-doped ferrite catalyst from Cr-containing electroplating sludge with activated persulfate for efficient degradation of tetracycline. *J. Environ. Chem. Eng.* **2022**, *10*, 108805. [[CrossRef](#)]
25. GB7467-87; Water Quality-Determination of Hexavalent Chromium-Diphenylcarbazide Spectrophotometric Method. National Environmental Protection Agency; Beijing, China, 1987.
26. GB/T15555.4-1995; Solid Waste-Determination of Hexavalent Chromium-Diphenylcarbazide Spectrophotometric Method. National Environmental Protection Agency; Beijing, China, 1995.
27. Pasupulety, N.; Alzahrani, A.A.; Daous, M.A.; Alhumade, H. CO₂-FT activity of Fe₇C₃ in FeZnK/ZrO₂ catalysts synthesized by using citric acid: Effect of pretreatment gas. *Fuel* **2024**, *360*, 130596. [[CrossRef](#)]
28. Shao, J.; Yuan, X.; Leng, L.; Huang, H.; Jiang, L.; Wang, H.; Chen, X.; Zeng, G. The comparison of the migration and transformation behavior of heavy metals during pyrolysis and liquefaction of municipal sewage sludge, paper mill sludge, and slaughterhouse sludge. *Bioresour. Technol.* **2015**, *198*, 16–22. [[CrossRef](#)]
29. Huang, H.-J.; Yuan, X.-Z. The migration and transformation behaviors of heavy metals during the hydrothermal treatment of sewage sludge. *Bioresour. Technol.* **2016**, *200*, 991–998. [[CrossRef](#)] [[PubMed](#)]
30. Liao, C.-Z.; Tang, Y.; Lee, P.-H.; Liu, C.; Shih, K.; Li, F. Detoxification and immobilization of chromite ore processing residue in spinel-based glass-ceramic. *J. Hazard. Mater.* **2017**, *321*, 449–455. [[CrossRef](#)] [[PubMed](#)]
31. Zhang, J.; Xie, W.; Chu, S.; Liu, Z.; Wu, Z.; Lan, Y.; Galvita, V.V.; Zhang, L.; Su, X. Sufficient extraction of Cr from chromium ore processing residue (COPR) by selective Mg removal. *J. Hazard. Mater.* **2022**, *440*, 129754. [[CrossRef](#)]
32. Zhou, J.; Liu, X.; Zheng, J.; Li, L.; Liu, W.; Lin, L.; Lin, Z. Simultaneous separation and immobilization of Cr(VI) from layered double hydroxide via reconstruction of the key phases. *J. Hazard. Mater.* **2021**, *416*, 125807. [[CrossRef](#)]
33. Xiao, C.; Li, S.; Yi, F.; Zhang, B.; Chen, D.; Zhang, Y.; Chen, H.; Huang, Y. Enhancement of photo-Fenton catalytic activity with the assistance of oxalic acid on the kaolin-FeOOH system for the degradation of organic dyes. *Rsc Adv.* **2020**, *10*, 18704–18714. [[CrossRef](#)] [[PubMed](#)]
34. Xin, S.; Tang, Y.; Jia, B.; Zhang, Z.; Li, C.; Bao, R.; Li, C.; Yi, J.; Wang, J.; Ma, T. Coupling Adsorbed Evolution and Lattice Oxygen Mechanism in Fe-Co(OH)₂/Fe₂O₃ Heterostructure for Enhanced Electrochemical Water Oxidation. *Adv. Funct. Mater.* **2023**, *33*, 2305243. [[CrossRef](#)]
35. Zhang, B.; Wang, L.; Zhang, Y.; Ding, Y.; Bi, Y. Ultrathin FeOOH Nanolayers with Abundant Oxygen Vacancies on BiVO₄ Photoanodes for Efficient Water Oxidation. *Angew. Chem. -Int. Ed.* **2018**, *57*, 2248–2252. [[CrossRef](#)] [[PubMed](#)]
36. Park, D.; Yun, Y.-S.; Park, J.M. XAS and XPS studies on chromium-binding groups of biomaterial during Cr(VI) biosorption. *J. Colloid Interface Sci.* **2008**, *317*, 54–61. [[CrossRef](#)]
37. Bagus, P.S.; Nelin, C.J.; Brundle, C.R.; Crist, B.V.; Lahiri, N.; Rosso, K.M. Covalency in Fe₂O₃ and FeO Consequences for XPS satellite intensity. *J. Chem. Phys.* **2020**, *153*, 194702. [[CrossRef](#)] [[PubMed](#)]
38. Bagus, P.S.; Nelin, C.J.; Brundle, C.R.; Crist, B.V.; Lahiri, N.; Rosso, K.M. Combined multiplet theory and experiment for the Fe 2p and 3p XPS of FeO and Fe₂O₃. *J. Chem. Phys.* **2021**, *154*, 094709. [[CrossRef](#)] [[PubMed](#)]
39. Raeburn, S.P.; Ilton, E.S.; Veblen, D.R. Quantitative determination of the oxidation state of iron in biotite using X-ray photoelectron spectroscopy: II. In situ analyses. *Geochim. Cosmochim. Acta* **1997**, *61*, 4531–4537. [[CrossRef](#)]
40. Lotfian, N.; Nourbakhsh, A.; Mirsattari, S.N.; Saberi, A.; Mackenzie, K.J.D. A comparison of the effect of nanostructured MgCr₂O₄ and FeCr₂O₄ additions on the microstructure and mechanical properties of direct-bonded magnesia-chrome refractories. *Ceram. Int.* **2020**, *46*, 747–754. [[CrossRef](#)]
41. Downie, L.J.; Goff, R.J.; Kockelmann, W.; Forder, S.D.; Parker, J.E.; Morrison, F.D.; Lightfoot, P. Structural, magnetic and electrical properties of the hexagonal ferrites MFeO₃ (M=Y, Yb, In). *J. Solid State Chem.* **2012**, *190*, 52–60. [[CrossRef](#)]
42. Wu, C.; Tu, J.; Tian, C.; Geng, J.; Lin, Z.; Dang, Z. Defective magnesium ferrite nano-platelets for the adsorption of As(V): The role of surface hydroxyl groups. *Environ. Pollut.* **2018**, *235*, 11–19. [[CrossRef](#)]
43. Bourzami, R.; Guediri, M.K.; Chetoui, A.; Messai, Y.; Benkouachi, O.R.; Chebli, D. Design a Novel Type-II Heterojunction SnO₂-FeTiO₃ Decorated with Metallic Ag⁰. Effect of Electronic and Structural Properties on Adsorptive and Photocatalytic under Visible Light Performances. *Russ. J. Phys. Chem. A* **2023**, *97*, 2682–2692. [[CrossRef](#)]

44. Sharma, M.; Rani, J.; Bhardwaj, S.; Agrawal, A.; Ghosh, R.K.; Kuanr, B.K. Effect of annealing temperature on structural, optical, magnetic and electrical properties of CrFeO₃ multiferroic nanoparticles: A validation to first-principle calculations. *J. Alloys Compd.* **2022**, *929*, 167338. [[CrossRef](#)]
45. Franken, T.; Heel, A. Are Fe based catalysts an upcoming alternative to Ni in CO₂ methanation at elevated pressure? *J. CO₂ Util.* **2020**, *39*, 101175. [[CrossRef](#)]
46. Seuser, G.; Martinelli, M.; Garcia, E.S.; Upton, G.F.; Ayala, M.; Villarreal, J.; Rajabi, Z.; Cronauer, D.C.; Kropf, A.J.; Jacobs, G. Reverse water-gas shift: Na doping of m-ZrO₂ supported Pt for selectivity control. *Appl. Catal. A-Gen.* **2023**, *650*, 119000. [[CrossRef](#)]
47. Shen, C.; Sun, K.; Zhang, Z.; Rui, N.; Jia, X.; Mei, D.; Liu, C.-J. Highly Active Ir/In₂O₃ Catalysts for Selective Hydrogenation of CO₂ to Methanol: Experimental and Theoretical Studies. *Acs Catal.* **2021**, *11*, 4036–4046. [[CrossRef](#)]
48. Xie, H.; Liu, N.; Huang, J.; Chen, S.; Zhou, G. CoCe composite catalyst for the CH₄/CO₂ reforming reaction: Synergistic effects between Co and Ce species. *J. Energy Inst.* **2023**, *111*, 101389. [[CrossRef](#)]
49. Liu, Y.; Liu, Q.; Chen, M.; Ma, L.; Yang, B.; Chen, J.; Lv, Z.; Liang, Q.; Yang, P. Evaluation of migration of heavy metals and performance of product during co-pyrolysis process of municipal sewage sludge and walnut shell. *Environ. Sci. Pollut. Res.* **2017**, *24*, 22082–22090. [[CrossRef](#)]
50. Liu, J.; Zhang, X.-H.; Tran, H.; Wang, D.-Q.; Zhu, Y.-N. Heavy metal contamination and risk assessment in water, paddy soil, and rice around an electroplating plant. *Environ. Sci. Pollut. Res.* **2011**, *18*, 1623–1632. [[CrossRef](#)]

Disclaimer/Publisher's Note: The statements, opinions and data contained in all publications are solely those of the individual author(s) and contributor(s) and not of MDPI and/or the editor(s). MDPI and/or the editor(s) disclaim responsibility for any injury to people or property resulting from any ideas, methods, instructions or products referred to in the content.